



A New Approach to Evaluate 3D Flow Fields Using an Off-Axis 2D PIV System: Investigation of a Tubular Reactor Equipped with Kenics Static Mixers

Z. Yao¹ · F. Alberini² · G. Montante² · A. Paglianti²

Received: 21 October 2022 / Accepted: 31 January 2023
© The Author(s) 2023

Abstract

In this work, an off-axis 2D Particle Image Velocimetry system is used to obtain the 3D flow field at the outlet of a tubular reactor equipped with Kenics static mixers. The 3D flow fields are obtained exploiting the out-of-plane velocity component and considering the symmetrical features of the flow generated by the static mixers. The raw results show that the velocity vectors, measured on a cross section perpendicular to the tube axis by 2D-PIV with the camera located at 24° from the measurement plane, are affected by the axial component of the flow. However, taking into account the symmetry of the flow field with respect to the tubular reactor axis and evaluating the effect of the out of plane velocity component, the correct 2D velocity vectors on the plane and also the velocity component in the axial direction can be calculated from the raw 2D PIV data. The consistency of the methodology is demonstrated by comparison of the results with the flow field measured in a smaller tubular reactor of similar geometry and Reynolds number with a symmetrical 2D-PIV system, with the camera located perpendicularly to the laser plane. Then, the 3D features of the flow are analyzed to characterize the effects of the different combinations of static mixer configurations on the fluid dynamics of the system in turbulent conditions. The results show that, as the pressure drop increases, a more uniform velocity distribution is achieved.

Keywords Mixing · Kenics · PIV · Turbulence · 3D Flow field

Introduction

Static mixers (also called motionless mixers) are mixing devices that contain no moving parts and are mainly used for continuous mixing of fluids [1]. They are an attractive alternative to conventional batch agitation system, due to their higher potential efficiency in term of energy consumption per unit volume [2]. The small footprint, low equipment operation and maintenance costs, sharp residence time distribution, improved selectivity through intensified mixing and isothermal operation, byproduct reduction, and enhanced safety are some of the main features that have promoted the

use of these devices in chemical, pharmaceutical, food processing, polymer synthesis, pulp and paper, paint and resin, water treatment, and petrochemical industries [2–8]. Further attention is attracted from static mixer, since the Paris Climate Agreement, that pushed many countries towards lower power consumption and environmental protection.

Kenics static mixers (KSM), as one of the classic types of static mixers, have the advantages of their unique structure and easy manufacturing [9]. In the early stages, [10, 11] studied mass transfer characteristics in KSM by measuring the rate of naphthalene evaporation. Pustenlik [12] and Kemblowski and Pustelnik [13] proposed residence time distribution model in KSM. Ling and Zhang [14] used helical coordinates to calculate velocity field in KSM, and the impacts of twist angle and aspect ratio of a mixing element on mixing efficiency were obtained. The mixing performance of KSM has been also investigated by finite element and Lagrangian methods [15–18]. Jaffer and Wood [19] studied laminar flow field in KSM through laser induced fluorescence. In a review of Thakur

✉ F. Alberini
federico.alberini@unibo.it

¹ School of Construction Machinery, Chang'an University, Xi'an 710064, China

² Department of Industrial Chemistry 'Toso Montanari', University of Bologna, via Terracini 34, 40131 Bologna, Italy



et al. [2], the industrial applications of static mixers in last century were summarized.

Recently, with the improvement of computing power and the development of computational fluid dynamics (CFD) methods, more and more researchers explored pressure drop and mixing performance of static mixers by means of numerical simulation [20]. Van Wageningen et al. [21] investigated the flow characteristics in KSM in the range of Reynolds number (Re) = 100 ~ 1000 through CFD simulations. Song and Han [22] proposed a pressure drop correlation in KSM through CFD calculations, which was validated by the comparison with various pressure drop data reported in the literature. Kumar et al. [23] explored flow patterns and mixing behavior in KSM over a wide range of $Re = 1 \sim 25,000$ through CFD methods. Lisboa et al. [24] employed standard $k-\epsilon$, RNG $k-\epsilon$ and $k-\omega$ to study the thermal efficiency of KSM for pre-heat supercritical carbon dioxide. Meng et al. [25] evaluated heat transfer performance of KSM using CFD. Jiang et al. [26] studied the effect of aspect ratio on mixing performance and the effect of element thickness on pressure drop in KSM by CFD simulations. Nyande et al. [27] employed CFD simulations to obtain mixing performance and pressure drop in a modified design of KSM under laminar flow conditions.

Compared with numerical simulation, experiments for the flow field in KSM are relatively scarce. Peryt-Stawiarska and Jaworski [28] and Murasiewicz and Jaworski [29] obtained velocity profiles in KSM using laser doppler anemometer. Alberini et al. [30, 31] and Ramsay et al. [32] employed planar laser induced fluorescence and image processing method

to evaluate KSM mixing performance. Rafiee et al. [33] used positron emission particle tracking technique to study laminar flow of a high viscosity Newtonian and non-Newtonian fluids in KSM.

As well known, PIV (Particle Image Velocimetry) has been extensively used for the fluid dynamics investigation of many equipment of the chemical process industry [34–36] mainly adopting a standard arrangement of the instrumentation with the camera located in front of the measurement plane. In a previous work by Yoon and Lee [37], the importance of the perspective error caused by the out-of-plane motion was discussed. A stereoscopic particle image velocimetry (SPIV) measurements were compared against the 2D PIV results to show this effect.

In recent years, some efforts have been oriented to measure three-dimensional flow fields by using a single camera. Noto and Tasaka [38] developed a new approach that allows to determine the out of plane component by using a single-color camera and two differently colored laser sheets. Xiong et al. [39] proposed the so called RainbowPIV that consists of an illumination module to generate a rainbow pattern, for catching the distance of particles from the camera and a software analysis that allows to reconstruct the velocity vector fields. Other contributions [40, 41] are based on the work by Willert and Gharib [42], in which a single camera system uses defocusing in conjunction with a mask embedded in the camera lens to decode three-dimensional point sources of light on a single image. The latter method has the disadvantage of using low particle seeding density due

Fig. 1 Sketch of the rig and KSM: (a) Overall schematic; (b) KSM Static mixer element

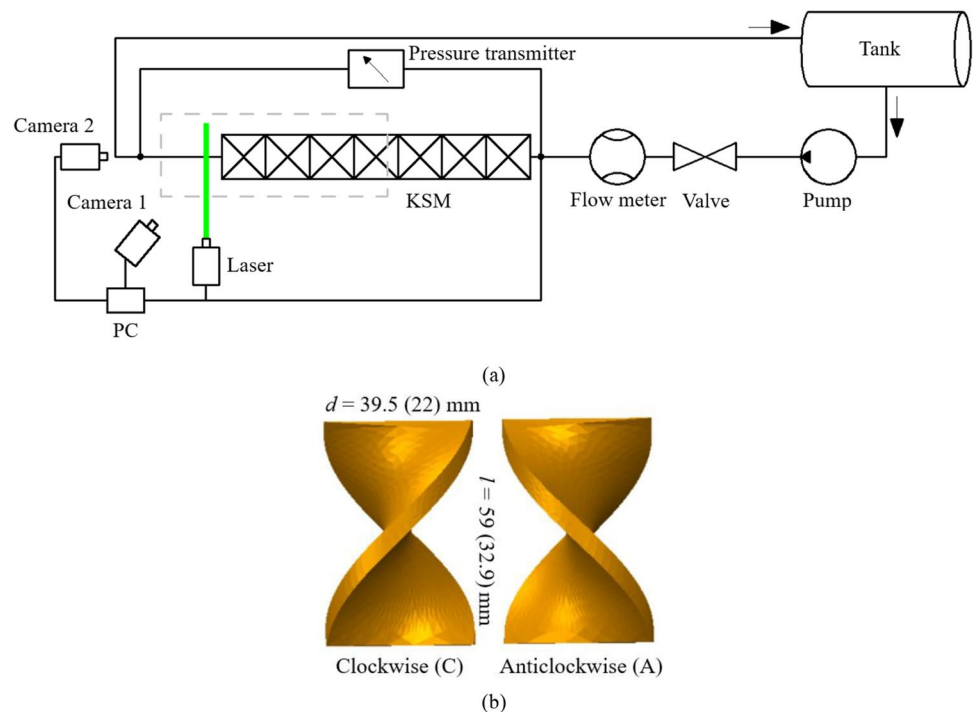


Table 1 Static mixer configurations for this work, considering the flow form right to left

Configurations	C		C-C	
	C-A		A	
	A-A		A-C	
	7×C			

to the difficulty of distinguishing overlapping patterns from nearby particles.

In this work, we exploit the effect of the out-of-plane motion to develop a new methodology to measure the three dimensional mean velocity field by a single camera in a symmetrical flow. The new methodology is applied to a tubular reactor and the consistency of the results is assessed by data collected in a smaller tubular reactor of similar geometry which allowed the acquisition of the flow field by a 2D PIV system with a standard arrangement of the camera with respect to the laser light sheet. For this purpose, a turbulent fluid flow regime is selected. The new methodology together with the pressure drop data is adopted to investigate the effect of clockwise or/and anticlockwise configurations and of the number of elements on the mixing characteristics of the tubular reactor.

Materials and Methods

Experimental Rig

The investigation was carried out adopting two different tubular reactors made of Perspex equipped with variable number and types of Kenics static mixers. The bigger one has an inner diameter, D , equal to 39.5 mm, and length, L , of 7 m, while for the smaller D and L were equal to

Table 2 Re and flow rate used for pressure drop measurements

Flow rate [m ³ /h]	1.12	2.13	3.27	4.19	7.34
Re	9994	18997	29259	37421	65625

22 mm and 1.25 m, respectively. Figure 1(a) shows an overall schematic of the experimental rig used in this work [43]. The rig consists of a storage tank filled with water at ambient temperature, which feeds a centrifugal pump (Robuschi, Italy). The pump delivers the selected flow rates, controlled by a flowmeter (Yokogawa, Germany), to the tubular reactors. Details about the PIV systems and configurations will be reported later.

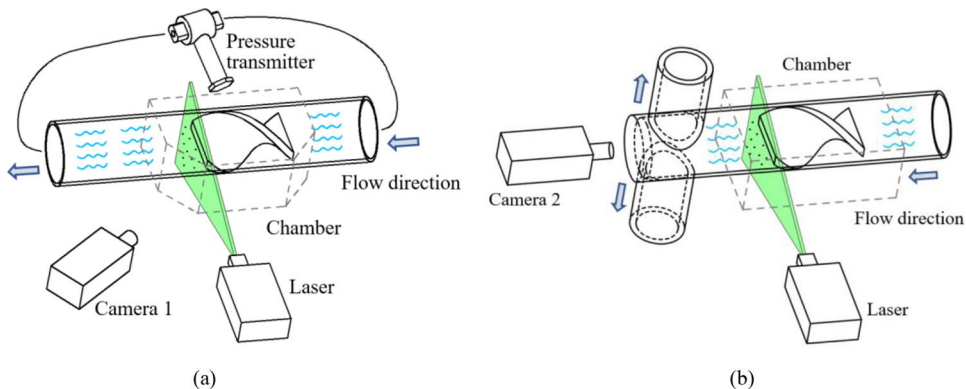
As inserts of the tubular reactors, two types of KSM have been used, clockwise (C) and anticlockwise (A), as shown in Fig. 1(b). The static mixers were manufactured using a 3D printer (Guider IIs, Flashforge, China), and the length and diameter of a single element were $l = 59$ and 32.9 mm and $d = 39.5$ and 22 mm for the larger and the smaller tubular reactor, respectively. In both cases, the ratio between the length of the mixer element and the pipe diameter was 1.5.

The investigated configurations are listed in Table 1.

Operating Conditions

The Reynolds number (Re) is defined as

Fig. 2 PIV system: (a) System 1; (b) System 2



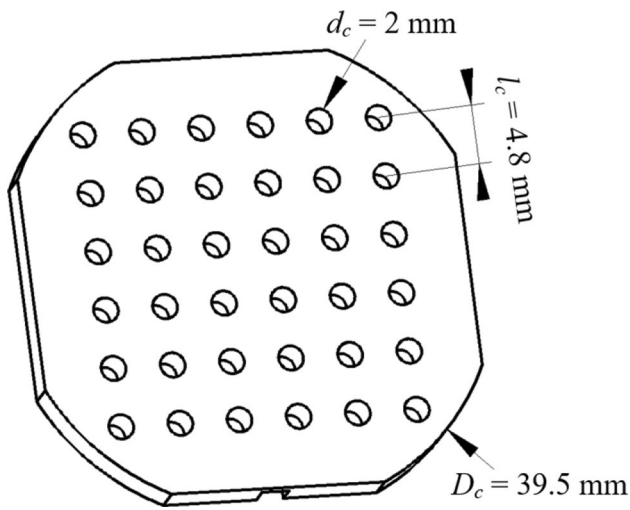


Fig. 3 Sketch of the target for calibration in the PIV measurement

$$Re = \frac{Dv\rho}{\mu} \quad (1)$$

where ρ , μ and v are the density, the viscosity and the superficial velocity of the fluid, respectively. In the following, Re is calculated at the inlet, based on the empty pipe velocity as in previous works [17, 44]. For the PIV measurements, the flow rates of water, which was the fluid adopted for the investigation, were $1.12 \text{ m}^3 \cdot \text{h}^{-1}$ (for $D_1 = 39.5 \text{ mm}$) and $0.59 \text{ m}^3 \cdot \text{h}^{-1}$ (for $D_2 = 22 \text{ mm}$). The corresponding Re were 9994 and 9468, respectively. The investigated flow rates and Re adopted in the pressure drop measurements, that were collected in the tubular reactor of $D = 39.5 \text{ mm}$, are reported in Table 2.

The Pressure Drop Measurements

The pressure drop was measured to identify differences in term of energy consumption among the different

configurations in the tubular reactor of $D = 39.5 \text{ mm}$. Pressure drop was measured by a differential pressure transmitter (PD-33X, Keller, Switzerland), enabling measurement at a sampling rate of 1 Hz. The experimental temperature was maintained at $20 \pm 2 \text{ }^\circ\text{C}$. The distance between the two pressure taps was 2.07 m.

The Particle Image Velocimetry Measurements

The PIV measurements were performed using a Dantec Dynamics system. The laser sheet source was a pulsed Nd: YAG laser (Solo I-15 Hz, New wave research, US), emitting light at 532 nm with a maximum frequency of 15 Hz. The images were captured by a Dantec PCO Camera with a pixel CCD, cooled by a Peltier module to improve the signal-to-noise ratio and equipped with a green filter to capture only the light emitted by the laser source. The laser control, the laser/camera synchronization and the data acquisition and processing were handled by a hardware module (FlowMap System Hub) and FlowManager software installed on a PC.

Two different arrangements of the instrumentation were adopted depending on the reactor used for the experimental investigation. Figure 2(a) shows the set up adopted for the reactor of $D = 39.5 \text{ mm}$, where the camera 1 was placed at an angle of 24° with respect to the pipe cross section. To avoid any disturbance due to inlet conditions, the measurement plane (system 1) was located at 2.07 m from the pipe inlet 2 mm from the outlet of the last static mixer used for each configuration used. The laser sheet was perpendicular to the axial direction, and the pipe was placed inside a Perspex chamber filled with water to minimize the laser diffraction effects due to the curvature of the pipe wall. Instead, as showed in Fig. 2(b) for the tubular reactor of $D = 22 \text{ mm}$, the laser light was still perpendicular to the axial direction, but the camera 2 was located perpendicularly adopting a window at the outlet of the pipe, similarly to the configuration

Fig. 4 Effect of the out-of-plane velocity component. (a) Raw flow field in the empty pipe; (b) Upper view of the investigated configuration

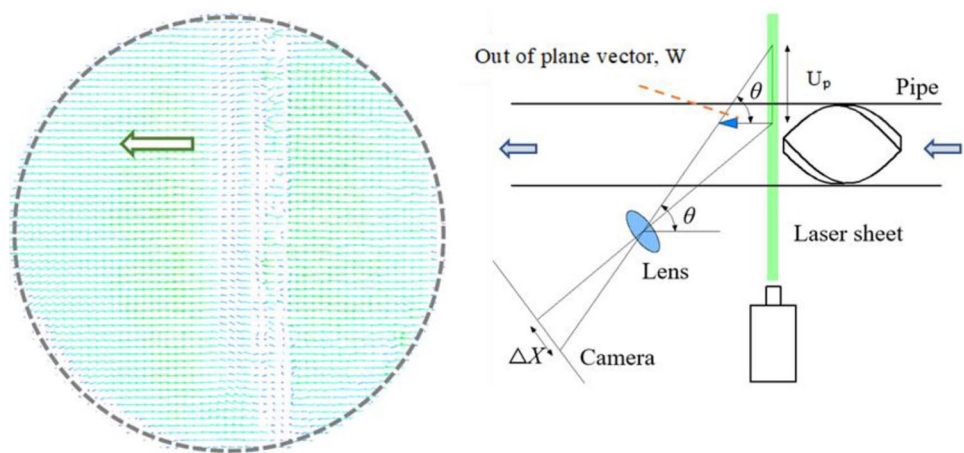
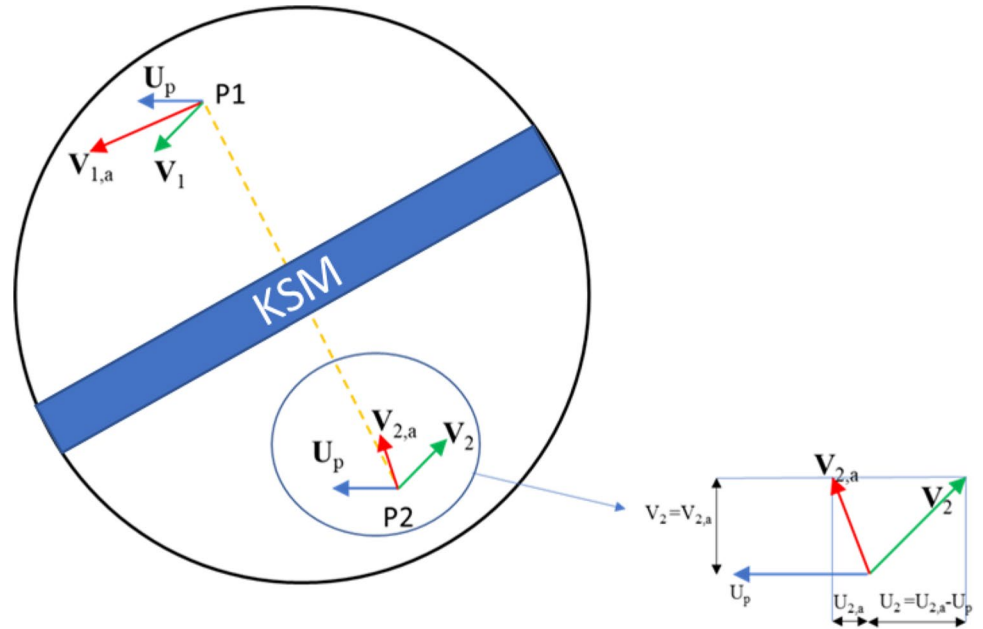


Fig. 5 Velocity components in two symmetrical points in cross section



used by Alberini et al. [30, 31]. The measurement plane was located at circa 5 diameters from the pipe outlet and, similarly to the other set up, 2 mm from the outlet of the last static mixer used for each configuration used. Moreover, to limit laser diffraction the chamber was a square solid piece of Perspex with in the middle a circular hole having the same cross-sectional area of the pipe. Finally, a double and symmetrical outlet configuration was engineered to minimize the outlet perturbations as shown in Fig. 2(b). The PIV measurements in the smaller reactor were performed to assess the analysis procedure devised to obtain the velocity field in the bigger tubular reactor.

In all cases, the liquid was seeded with Talco particles of mean diameter equal to $1.7 \mu\text{m}$ and the density of

2820 kg/m^3 [34]. The seeding particles concentration was carefully chosen in order to obtain from 5 to 10 particles for each interrogation area. The distance between laser sheet and the end of KSM was in all cases of a couple of mm, to avoid the laser reflections against the outlet of the static mixer.

For the flowrate equal to $1.12 \text{ m}^3 \cdot \text{h}^{-1}$, the time interval between two laser pulses, Δt , of $40 \mu\text{s}$ was selected based on the analysis of preliminary data collected with different values and the time interval which gave better vector validation results was selected. For the flow rate of $0.59 \text{ m}^3 \cdot \text{h}^{-1}$, the time interval was changed, inversely proportional to the superficial fluid velocity, for maintaining the same seeding particle displacement. For each run, a total number of image pairs of 800 was acquired; this number was selected since

Fig. 6 Identification of the center position in regions of high velocity magnitude

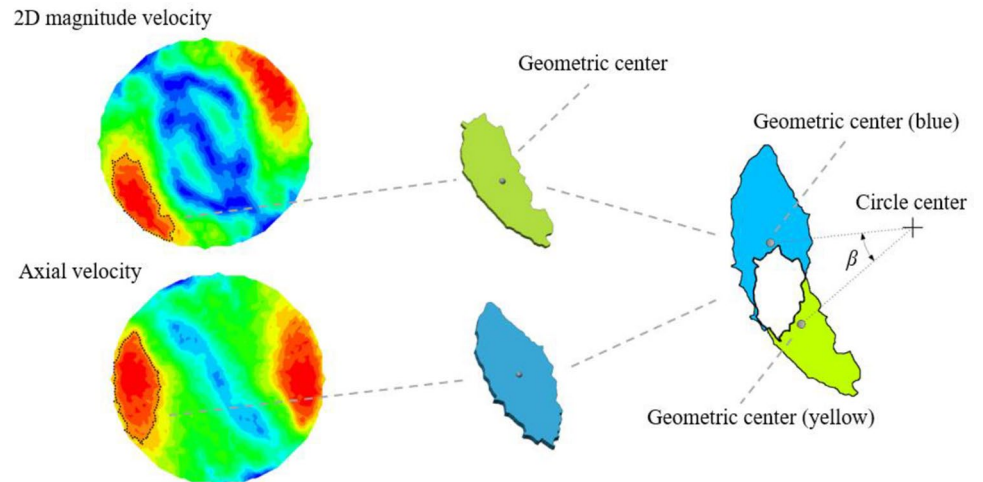
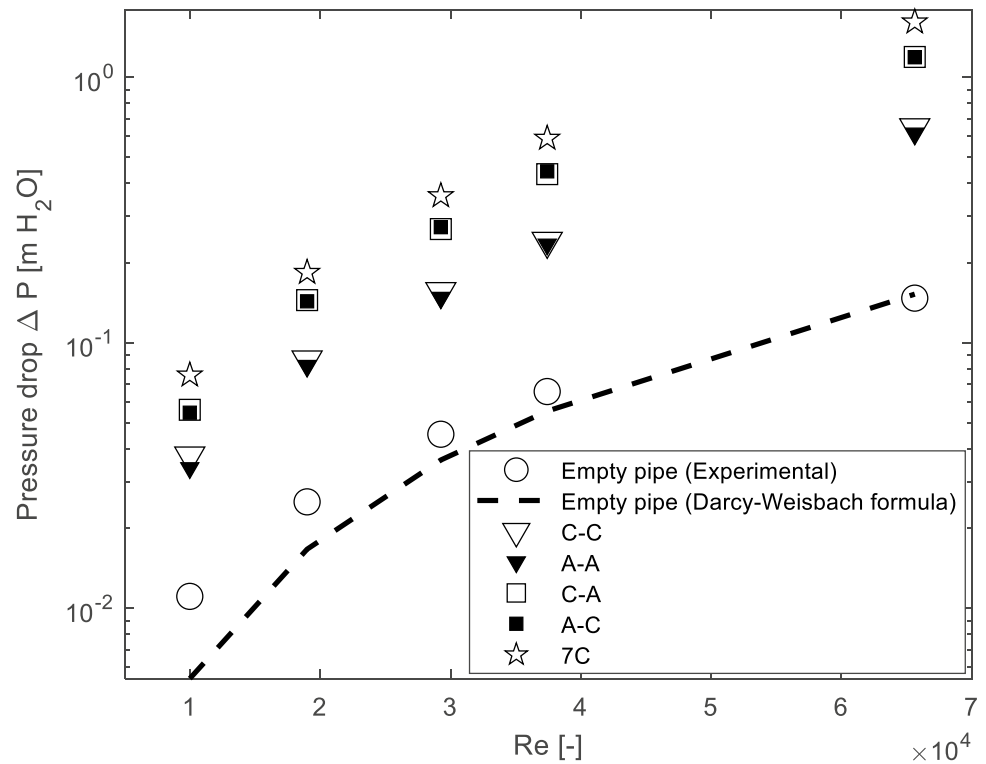


Fig. 7 Effect of mixing elements on pressure drop for the pipe diameter, $D_j = 39.5$ mm



it ensured the statistical independency of the mean velocity data. The acquisition frequency, between a pair of image to the next for the double frame camera was equal to 1 Hz for both configurations.

The velocity vector maps were obtained by applying the cross-correlation to the image pairs with an interrogation area size of 32×32 pixels (1.37×1.37 mm and 0.96×0.96 mm in the larger and the smaller tube, respectively) with overlap of 50%. The cross-correlation was applied after that the image obtained averaging the pixel intensity of the 800 images was subtracted from each image pair, to reduce the noise. The mean velocities were calculated from the instantaneous vectors that passed the validation procedure, i.e. vectors were discarded if they did not fulfill two conditions, one based on the evaluation of the peak heights in the correlation plane and the other on the velocity magnitude [34].

De-Warping and Out-of-Plane Velocity Components

Due to the impact of the angle between the camera and the tube axis, the images recorded with the off-axis camera by system 1 are affected from perspective misrepresentation by default, meaning that the relationship between the camera pixel and the real dimension is not constant across the measurement plane. With numerical models describing the perspective distortion (“warping”), it is however possible to compensate and correct (“de-warp”) the images adopting

suitable models to fit with targets of known geometrical characteristics [45]. The sketch of the target used for the calibration, which was manufactured by 3D printer, is shown in Fig. 3. The target, then, was inserted in the same position of the PIV measurement plane, and knowing the locations and the dimension of the holes it was possible to reconstruct the “de-warped” image which represents the perpendicular view of the target. This led us to obtain the algorithm to “de-warp” each PIV image and a calibration image which was used for the determination of pixel size calibration which was equal to $36.56 \mu\text{m}/\text{pixel}$.

However, with the de-warping of the image only the optical misrepresentation is addressed, and the misrepresentation induced by the out-of-plane velocity component W (axial direction) as depicted in Fig. 4(a) is not removed.

In particular, Fig. 4(a) shows the velocity field measured in an empty pipe after the de-warping step. The results show an accentuated horizontal component for all the vectors (directed from right to left) induced by the out of plane component associated in this flow system to the axial flow.

This was previously observed also by Yoon and Lee [37], where in their work, the out of plane component influenced the value of the in-plane components, obtained using 2D PIV measurements.

Referring to the investigated system of this work Fig. 4(b), the perspective error, induced by the out of plane velocity, is proportional to the angle θ , which is defined

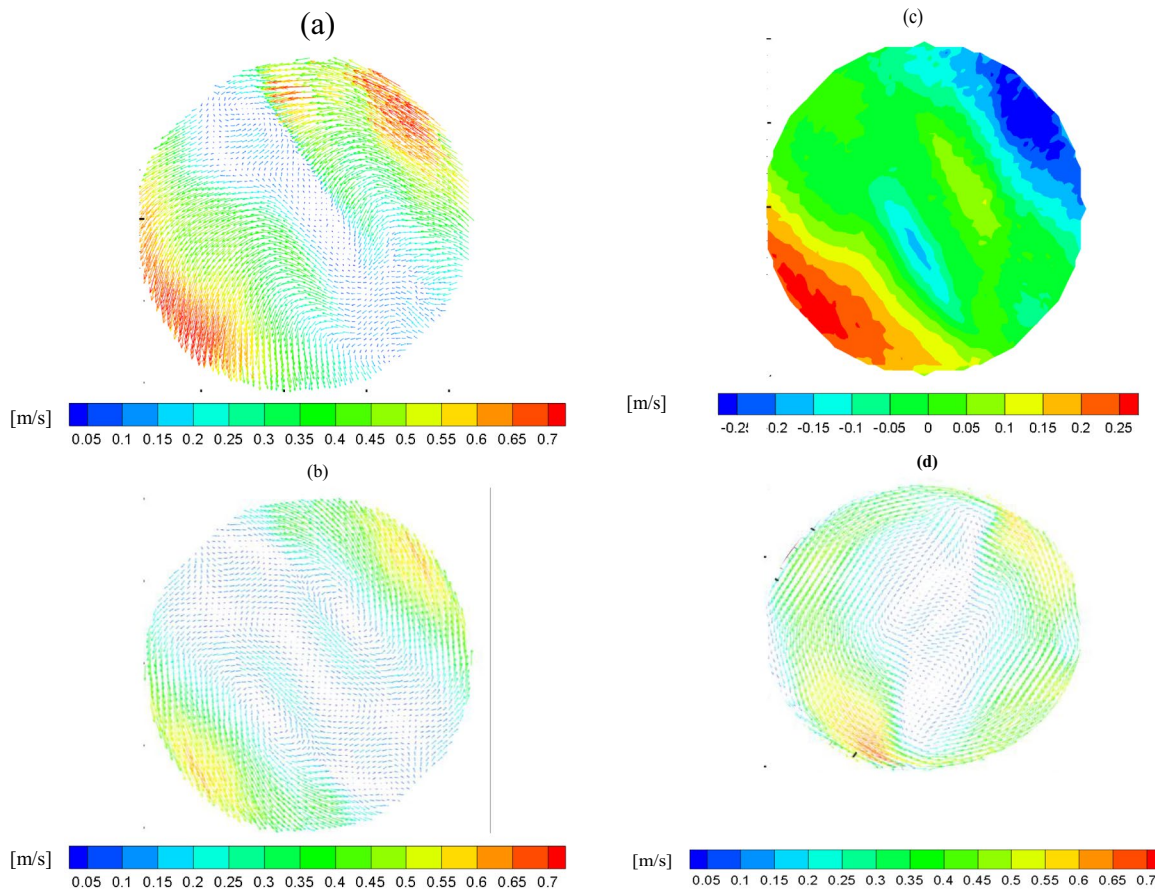


Fig. 8 2D velocity vector plot colored with the velocity magnitude in the “7×C” configuration: (a) Results for the larger tube (system 1) without out of plane correction; (b) Results for the bigger tube (system 1) with out of plane correction; (c) contour plot of the “raw” vertical component (system 1); (d) Results for the smaller tube (system 2)

as the angle between the measurement plane and the perspective plane.

In Fig. 4(b) it is schematized how the velocity, after de-wrapping, is also influenced by the out-of-plane component (axial component), W . This leads toward the misrepresentation for the particle displacements in the measurement plane, ΔX , which results into an accentuated horizontal velocity (U_p) on the plane. It is worthwhile noticing that, because the camera axis and the tube axis lay on the same horizontal plane, only the horizontal velocity component is influenced by W . Hence, the impact of W on horizontal velocity components is:

$$U_p = W \tan(\theta) \quad (2)$$

since U_p is the projection of the axial component in the horizontal direction.

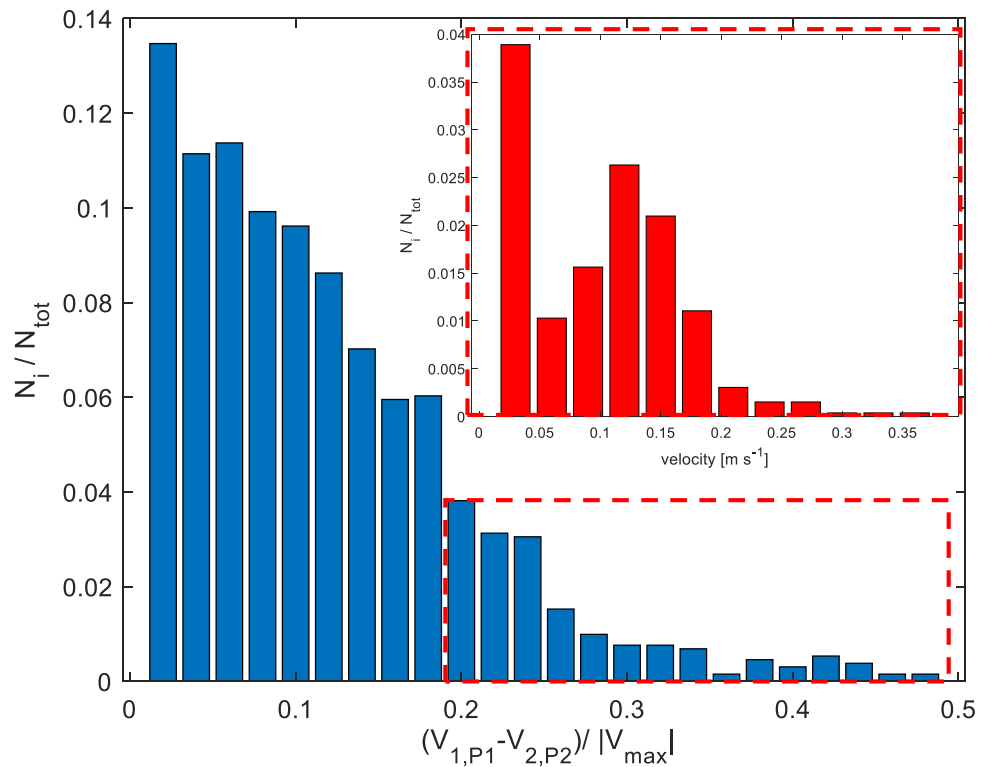
As a result, when the digital camera is inclined with respect to the pipe axis, in addition to the de-wrapping procedure required for correcting the perspective error

also the correction of the in-plane components has to be implemented.

However, this flow misrepresentation is used to estimate the intensity of the out of plane component, and this is possible, particularly, because the system of interest generates a symmetrical flow. As observed in previous work by Kumar et al. [23], the symmetrical flow, determined by the presence of KMS static mixers, is found at different regimens.

In Fig. 5, two symmetric points with respect to the measurement section center, $P1$ and $P2$ are considered. The data acquired by the off axis 2D-PIV system, after the de-wrapping step (similarly as shown in Fig. 4(b)), labelled as $V_{1,a}$ and $V_{2,a}$ are not symmetric, due to the effect of the projection of the out-of-plane component on the horizontal direction. However, in a symmetrical flow, like the one generated by KSM static mixers or empty pipe, the real velocity vectors resulting from the projection of the velocity vector on the measurement plane should be symmetric (hence $|V_1| = |V_2|$). Imposing this as a constrain, the out of plane component

Fig. 9 Distribution of normalized deviation between symmetrical points (as represented in Fig. 5) with the maximum velocity for the vertical component (in blue) for the “raw” vertical component, showed in Fig. 8(c); in red, the distribution of velocity intensities where the normalized deviation is above 20%



intensity for each vector location is extrapolated. This was possible selecting the reciprocal positions of the vectors according to their position respect to the wall of the static mixer in the cross section of the pipe, as depicted in Fig. 5.

Therefore, for obtaining the correct horizontal component of the velocity vector in the cross section, U_1 and U_2 , a correction should be applied to all pairs of vectors, considering the following relationship:

$$U_1 = U_{1,a} - U_p \quad (3)$$

$$U_2 = U_{2,a} - U_p \quad (4)$$

$$U_1 = -U_2 \quad (5)$$

where $U_{1,a}$ and $U_{2,a}$ are the raw velocity component in the horizontal direction.

In the following, exploiting this symmetric characteristic of the flow field in a pipe equipped with KSM, the combination of de-warping and correction for the effect of the out of plane components is applied for the evaluation of the 3D flow field by using a 2D PIV system.

Location of Velocity Peaks

To quantitatively compare the location of the zones with high velocity magnitude in the different static mixer

configurations, the geometric center of these zones was obtained by the software Creo 2.0, as shown in Fig. 6 fixing a velocity threshold. This exercise was repeated for all the experimental run. The analysis was then used to verify the effect of the different static element configurations.

Results and Discussion

The data analysis is split in five subsections; the results of the pressure drop will be presented in the first part. Then the results of the out of plane correction will be presented, followed by the analysis of the three velocity components. Final considerations will be presented in the last subsection considering the Coefficient of Variation and the frequency distribution of the 3D velocity magnitude.

Pressure Drop

Figure 7 shows the results of the pressure drop measurement, varying Re in the turbulent regime, for the different static mixer configurations for the pipe of diameter $D_I = 39.5$ mm. As reference point, the empty pipe pressure drop is also presented, which are consistent with the calculation by Darcy-Weisbach equation. Generally, it can be seen that very similar results are obtained for the C-C

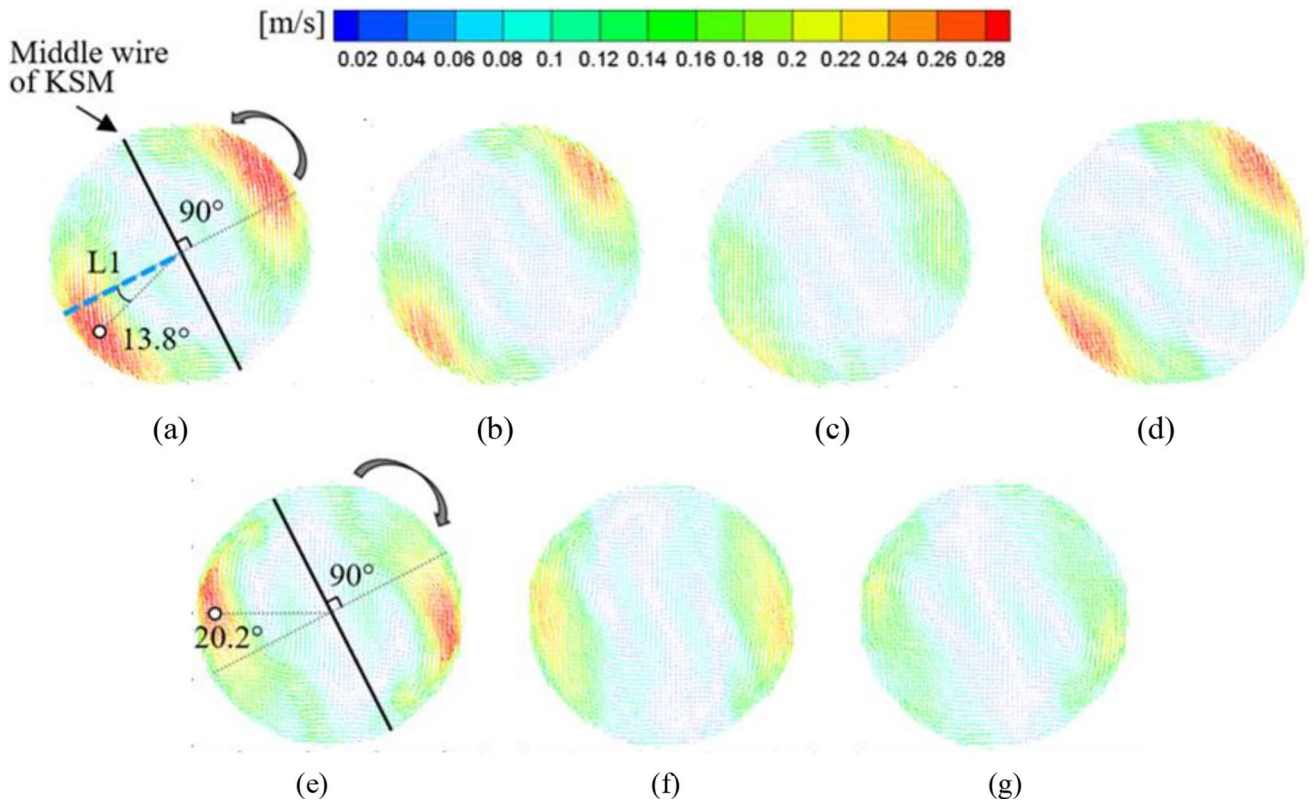


Fig. 10 2D velocity vector plot colored with the velocity magnitude for different configurations: (a) C; (b) C-C; (c) C-A; (d) 7×C; (e) A; (f) A-A; (g) A-C

Fig. 11 Comparison of radial profiles of velocity magnitude for different configurations

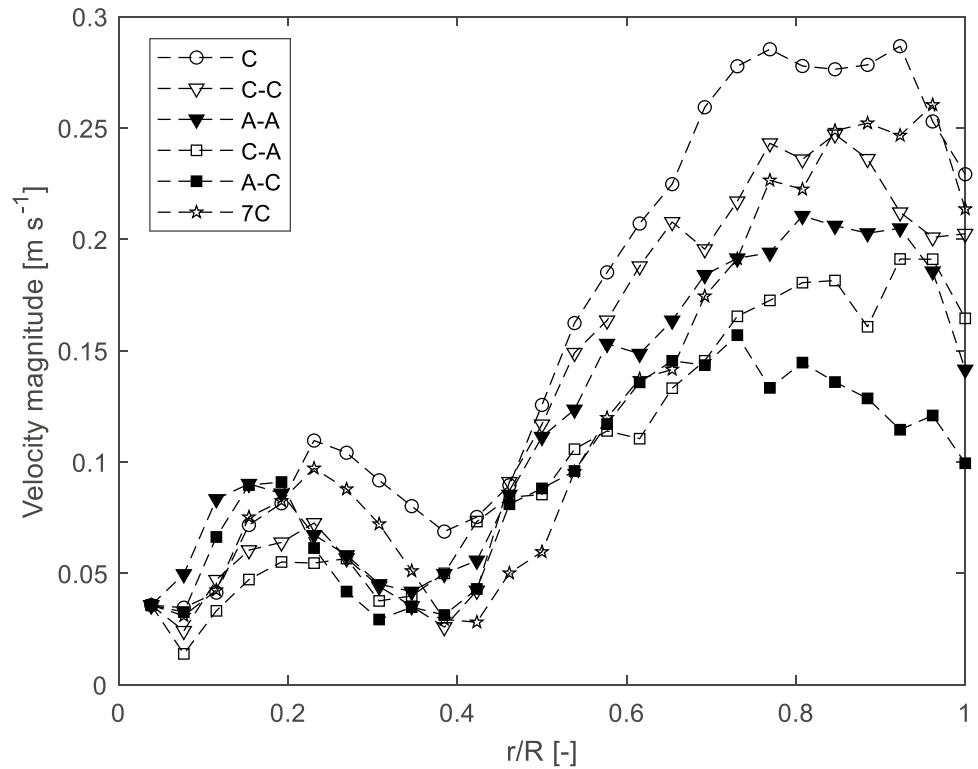


Fig. 12 Maps of tangential velocity for different configurations: (a) C; (b) C-C; (c) C-A; (d) 7×C; (e) A; (f) A-A; (g) A-C

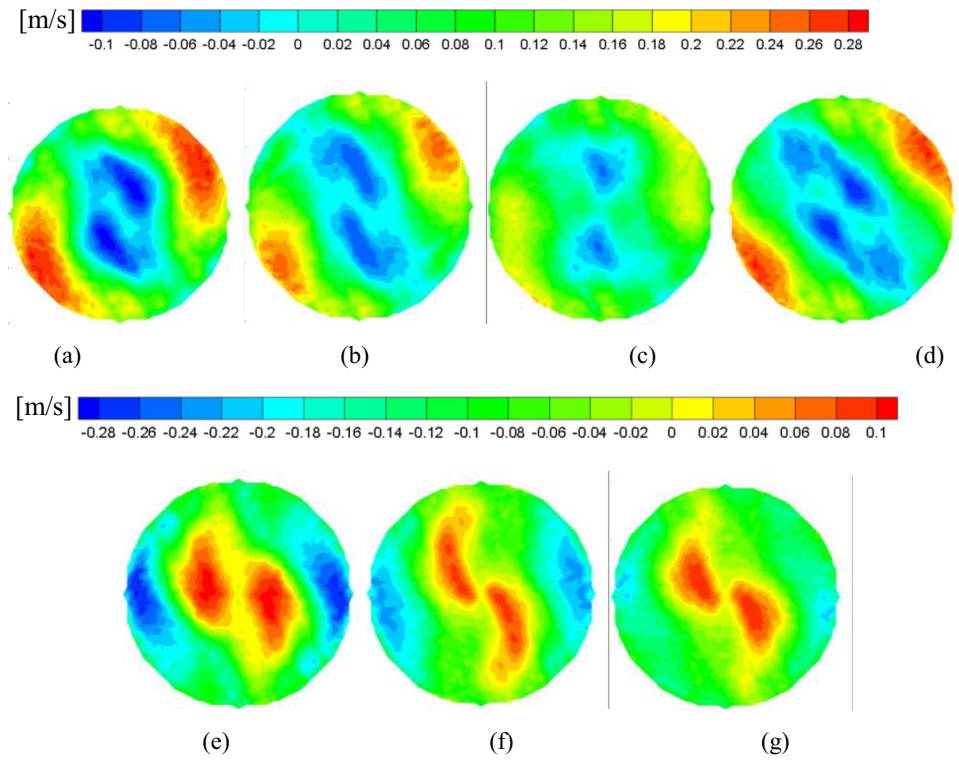


Fig. 13 Maps of radial velocity for different configurations: (a) C; (b) C-C; (c) C-A; (d) 7×C; (e) A; (f) A-A; (g) A-C

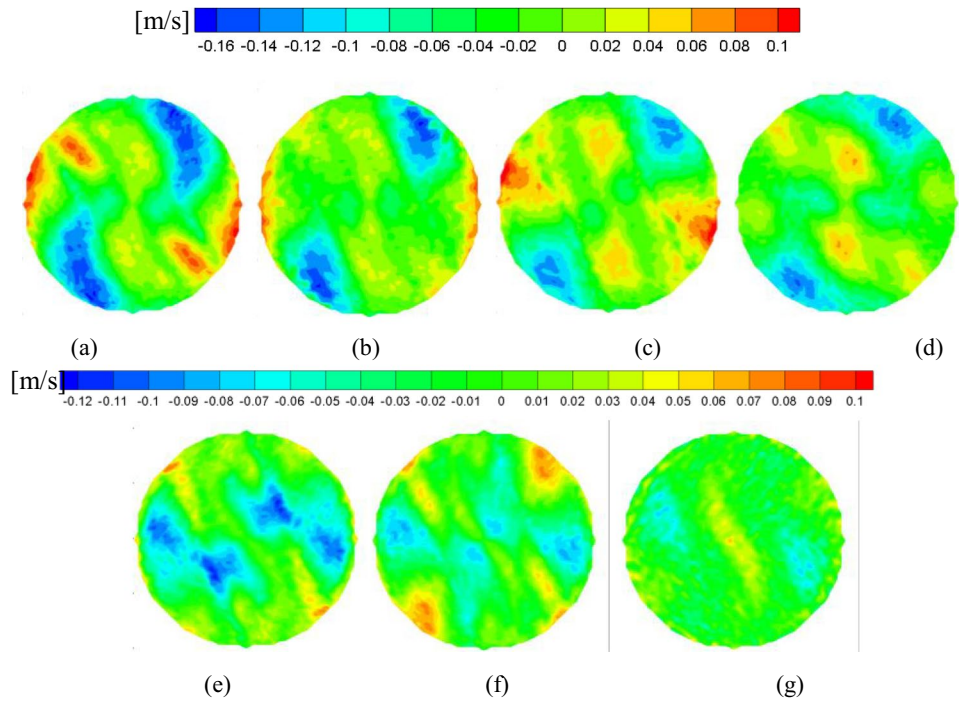


Fig. 14 Maps of axial velocity for different working conditions: (a) C; (b) C-C; (c) C-A; (d) 7×C; (e) A; (f) A-A; (g) A-C

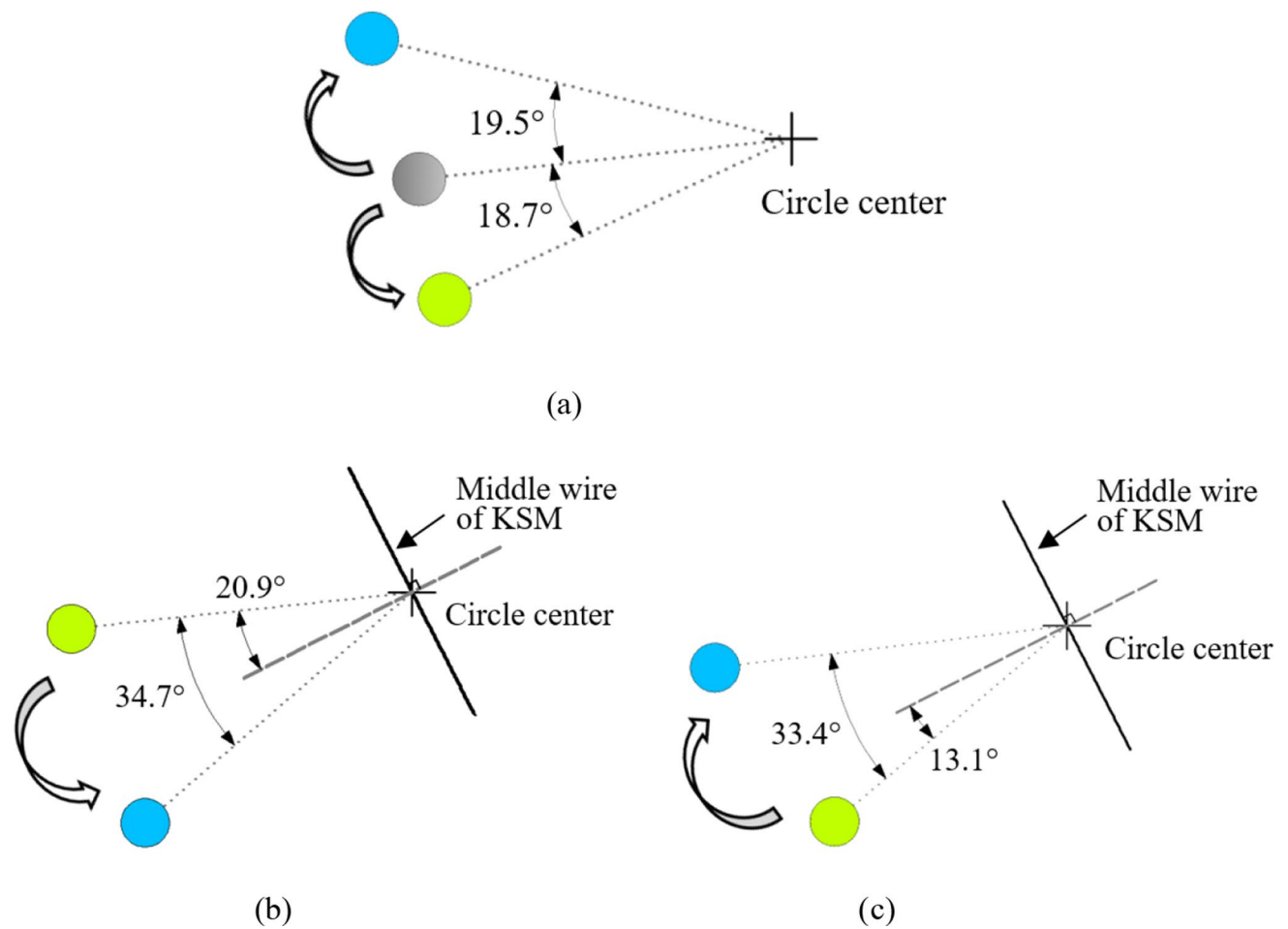
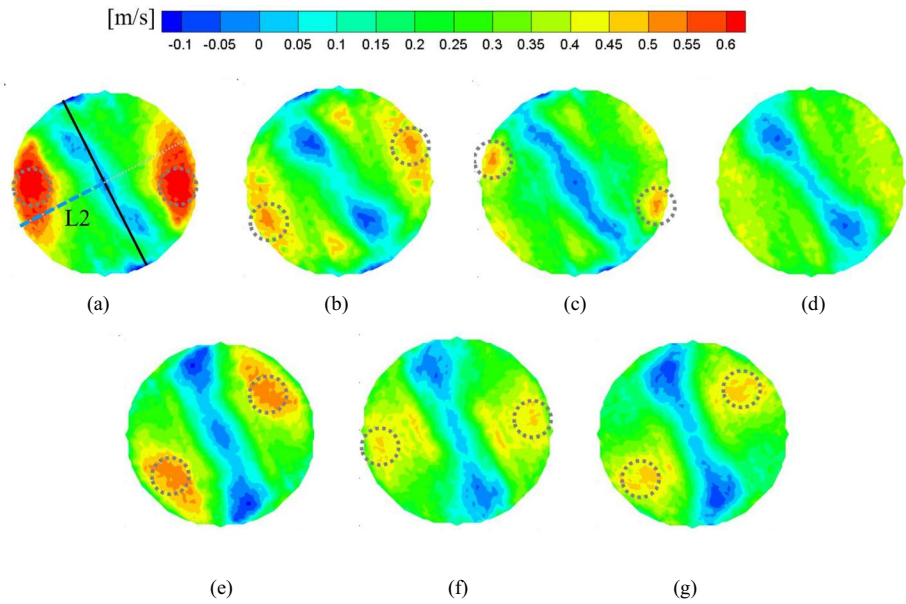


Fig. 15 Comparison of the position of center of the peak for axial velocity and 2D velocity magnitude: (a) Axial velocity C (grey), C-C (green), C-A (blue); (b) C set-up: 2D velocity magnitude (blue), axial velocity (green); (c) A set-up: 2D velocity magnitude (blue), axial velocity (green)

Fig. 16 Axial velocity in L2 of Fig. 13(a)

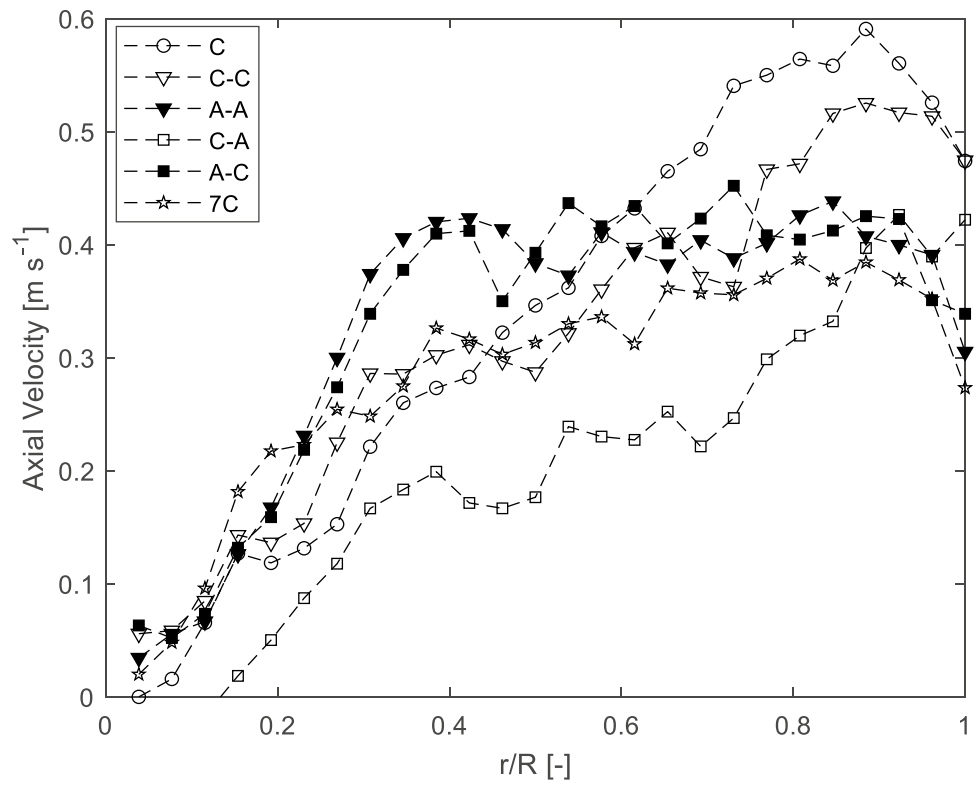


Fig. 17 Axial vorticity for different working conditions: (a) C; (b) C-C; (c) C-A; (d) $7 \times C$; (e) A; (f) A-A; (g) A-C

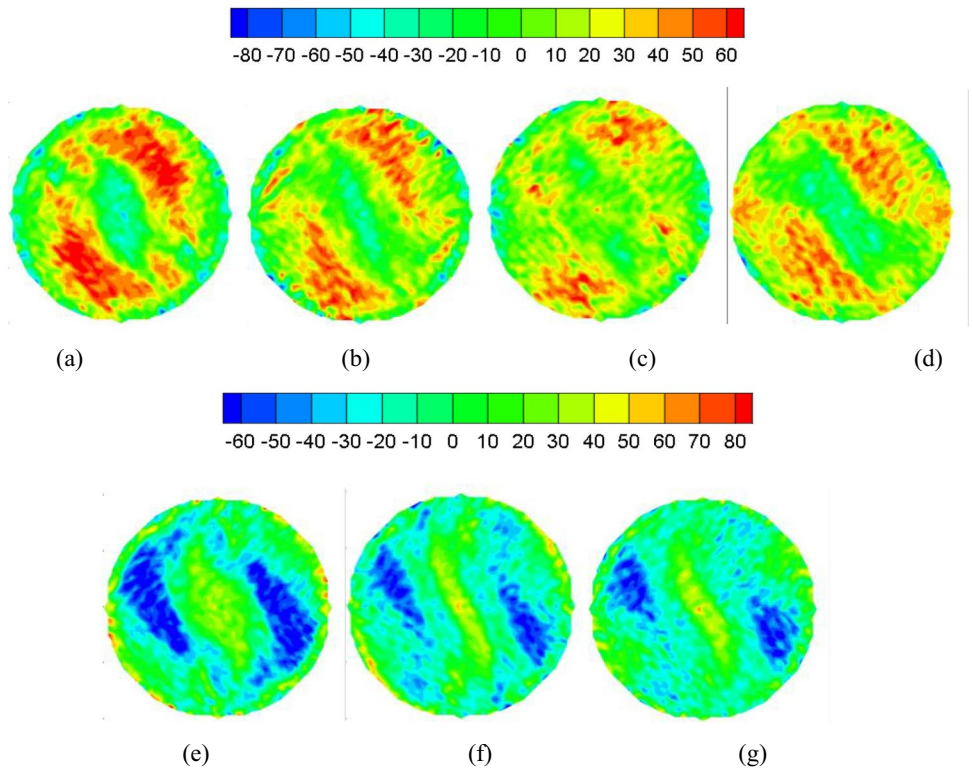
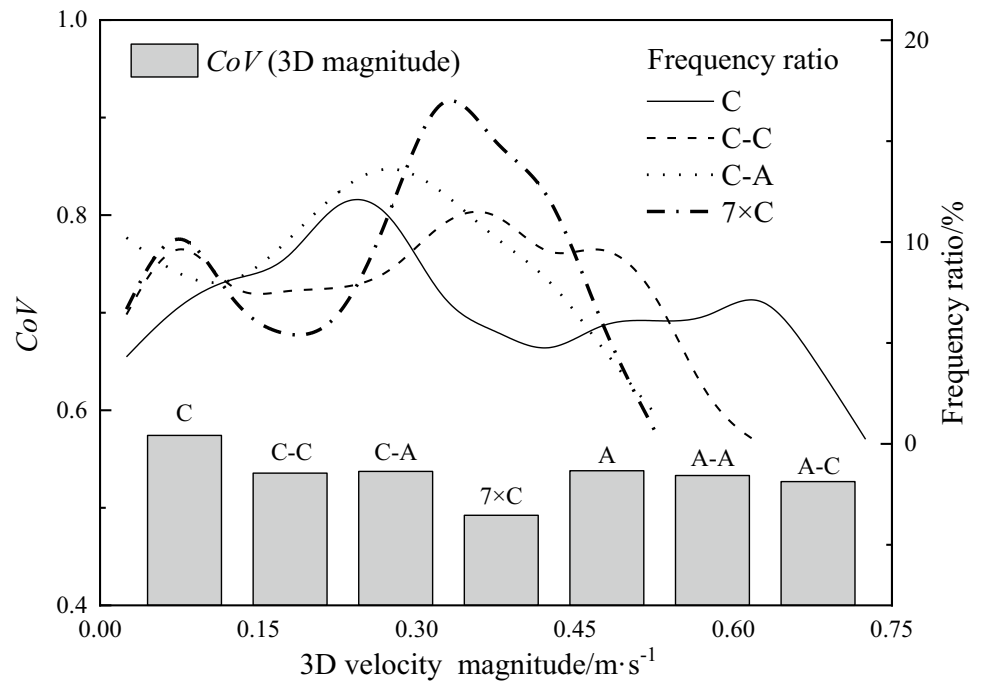


Fig. 18 3D velocity magnitude CoV and distribution for the different working conditions



and A-A combinations and for the C-A and A-C combinations. However, C-C (or A-A) vs C-A (or A-C) shows a significant difference. This suggests that the change of fluid direction, occurring between two static mixer elements generated by different rotation, has a significant impact on total pressure drop. The pressure drop measured with seven C elements are linearly dependent from the number of static elements.

2D Flow Field

Figure 8(a) and (b) show the 2D velocity vector plots obtained in the configuration “7×C” before and after the out of plane correction, respectively. The vectors of Fig. 8(a) are clearly affected by the fluid axial motion, which artificially increases the overall magnitude of the vectors and provides a strong monodirectional component of the flow. In Fig. 8(b) the correction of the out of plane component is applied. As can be observed, after the correction the flow field on the plane is symmetric, the velocity is stronger close the wall and weaker in the center, given the presence of the body of the static mixer.

Moreover, to further validate the assumption of symmetrical flow for the out of plane correction, in Fig. 8(c), the contour plot of the vertical “raw” component of the flow is presented for the same condition of Fig. 8(a-b). Clearly as shown, the vertical “raw” component is symmetric and it does not request any correction because of the effect of the presence of the out of plane component. To be noticed,

because of the position of the camera and the laser sheet the out of plane component influences only the horizontal “raw” component. This further justifies the assumption made in §2.5 (Fig. 5).

As qualitative comparison, Fig. 8(d) shows the 2D velocity vector plot obtained by the PIV system 2 in the smaller tube at similar Re , in this case the out of plane component was not removed because the measurement plane was perpendicular to the camera.

Despite the slightly different position of the downstream static mixer element, which is translated in an anticlockwise rotation of about 30° (in the smaller pipe Fig. 8(d) compared to the larger pipe in Fig. 8(b)), the overall flow pattern is similar between the two systems of reference. There are two stronger velocity peaks close to pipe wall, which is consistent with the results obtained through the PIV system 1 in the larger tube after the out of plane correction. In the center of the pipe, where the velocity magnitude is lower, small differences can be noticed comparing the data collected with the two systems, which can be attributed to unavoidable geometrical differences as, for instance, the element thickness at two different scales.

In order to quantify the incurred error using the proposed approach to remove the out of plane component, a direct comparison between the reciprocal points, for the two sides of the pipe cross section as schematized in Fig. 5, in term of the ‘raw’ vertical component is obtained. To quantify the deviation between the reciprocal points, the distribution of the deviation normalized with the maximum velocity for

the vertical component, is presented in Fig. 9 (in blue). As it can be seen, the majority of the reciprocal points have a relative deviation within 20% among the pairs. For the rest points (PIV cells (N), overall $\sim 10\%$ of the total number of PIV cells (N_{tot})), where the relative deviation is above 20%, it is also represented the distribution of velocity intensity (in red) at which these deviations occur. Clearly, the majority of the higher values of deviation occur for lower velocities and a for a very small number of points at high velocity. Overall it can be extrapolated from this analysis that the error on the estimation of the out of plane component is within the 20% deviation normalized against the superficial velocity ($|V_{\text{max}}|=0.33 \text{ m s}^{-1}$) for the majority of points, about 90% of total number of PIV cells. Moreover, as it will be presented in the following paragraphs, the maximum intensity of the out of plane component (axial component) is more than twice the superficial velocity in the high peak zones; hence the impact of the deviation between the reciprocal points in the vertical component (in term of relative error) will be less impactful on the overall estimation for the axial velocity.

Once verified that the correction for the out-of-plane component is valid, all the results presented in the following plots have been corrected to remove the effects of the out of plane component.

The 2D velocity vector plots obtained for the different configurations of the mixing elements are shown in Fig. 10. As can be observed, the turning direction of fluid depends on the geometric configuration of the final element (clockwise or anticlockwise). Stronger velocity peaks are found close to the wall of pipe, which are consistent with the data reported by Meng et al. [46] and Jiang et al. [47]. Moving from clockwise to anticlockwise configuration, the maximum of the velocity magnitude changes its position, as shown comparing the results of Fig. 10(a) with those reported in Fig. 10(e). The black thicker line in Fig. 10(a) and (e) represents the position of the static mixer blade at the outlet. The center of the higher velocity zone forms an angle of 13.8° below the perpendicular dashed line to the static mixer blade for the C configuration, and of 20.2° above the dotted line for the A configuration. This suggests that changing from a configuration to the other, the velocity peak rotates of about 34° .

Figure 11 shows the radial profile of the 2D velocity magnitude along the line L1 depicted in Fig. 10(a). For all the configurations, the velocity decreases towards the center, that correspond to the radial coordinate $r/R=0$. There are two velocity peaks with different magnitude depending on the specific configuration.

Tangential and Radial Velocity

The separate analysis of the tangential and radial velocity components, shown in Figs. 12 and 13 respectively,

allows to observe specific features obtained with the different configurations of the static mixers.

As can be observed from the tangential velocity distribution, the velocity peaks are close to the pipe wall, and weaker peaks with inverse direction are always located in the center. Comparing single elements C (A), with double elements C–C (A–A), as expected the peak intensities tend to decrease due to the impact of the subsequent element, which contributes to smooth the fluid velocity variations on the plane. Particularly in C–A (A–C), where the rotation of the flow is reversed, the peaks decrease even more. Similar observations can be drawn from the radial velocity maps. Generally, the pattern shown in Fig. 13 is more complex than that observed in Fig. 12, showing always zones of positive and negative velocities which have been noticed before also by Haddadi et al. [48].

Axial Velocity

The third component of the flow, that is the axial velocity component, has been calculated based on the equations presented in §2.5. Figure 14 shows the axial velocity maps for the different working conditions. The zones of high axial velocity are located close to the pipe wall, similarly to the 2D velocity magnitude shown in Fig. 10. The gradient of velocity across the section for the working condition $7 \times C$ is lower compared to the other cases which suggests a more uniform velocity distribution, going towards a plug flow type. The big step change is between one and two elements while the differences between C–C and $7 \times C$ are weaker.

Notably, the positions of peak of velocity, circled by grey lines in Fig. 14, change for the different working conditions because of the geometrical differences induced by the number and the shape of the elements. The location of the centers of the peaks in $7 \times C$ condition is not clear given the high uniformity of the velocity.

Figure 15(a) shows the quantitative comparison of the center positions of the velocity peak for the different working conditions. Each element has its own contribution to the location of this center.

For example, the C elements induce an anticlockwise rotation observed from a downstream view, therefore the addition to a C element of another C element upstream induces a rotation of the zone of maximum axial velocity (Fig. 15(a)). In this case the rotation is in the clockwise direction, the opposite effect is noticeable if an A element is added upstream the C element.

The center positions of peaks for the 2D velocity magnitude (radial and tangential) and the center positions for the axial peak velocity are compared in Fig. 15(b) and (c). The angles between the position of the peaks for the 2D velocity magnitude and the axial velocity is similar for these two

working conditions ((C) 34.7° vs. (A) 33.4°), but with the centers in the opposite positions as expected by the orientation of the rotation of the element. The angle between the peak position of axial velocity and the perpendicular line of middle wire of KSM is 20.9° for C and 13.1° for A.

Figure 16 illustrates the axial velocity along the L2 line (shown in Fig. 14(a)) that is located in the same position of L1. These profiles show that the velocity decreases toward the center, which is consistent with the numerical results obtained by Haddadi et al. [48], and the peaks of velocity decrease with the increase of number of elements or when elements with different orientation are employed, particularly in C-A (A-C) conditions.

Finally, the 2D vorticity (ω) component normal to the measurement plane, defined as:

$$\omega = \frac{dv}{dy} - \frac{du}{dx} \quad (6)$$

As shown in Fig. 17, it is evidenced the presence of clockwise rotating zones (Fig. 17(a), (b), (c), (d)) where the vorticity is positive and anticlockwise rotating zone (Fig. 17(e), (f), (g)) where the vorticity is negative. As can be observed, the vorticity magnitude of C and A is the highest and the high values are symmetric both respect to the pipe center. Compared with the results obtained with a single element, with the addition of one element of the same type, the vorticity magnitude is reduced. With the C-A and the A-C configurations, the maximum value of the vorticity and the extension of the high vorticity regions are smaller with respect to the other cases.

Overall Analysis of the Tubular Reactor Characteristics

To quantitatively compare the velocity flow patterns, the coefficient-of-variation (CoV) for the velocity in the cross section is calculated as:

$$CoV = \frac{\sqrt{\frac{\sum_{j=1}^m (v_j - \bar{v}_j)^2}{m-1}}}{\bar{v}_j} \quad (7)$$

where m is the number of the mean velocity vectors in the cross-section, v_j is the mean velocity magnitude in the interrogation area and \bar{v}_j is the average velocity magnitude in the cross section.

In addition, the frequency ratio of certain range of velocities in the measuring cross section is observed, defined as:

$$Fr_k = \frac{m_{k \sim k+0.05}}{m} \times 100\% \quad (8)$$

where $m_{k \sim k+0.05}$ is the number of mean velocity data between v_k and $v_k + 0.05$.

Figure 18 shows the CoV of the 3D velocity magnitude and the distribution of the frequency ratio for different working conditions, at the same liquid flowrate of 1.12 m³·h⁻¹. The CoV data show that the uniformity of velocity distribution increases when the number of elements is increased. The C set-up is that characterized by the higher value of CoV , while the lower value is observed for the 7×C set-up. Obviously, at a reduction of the CoV values, corresponds a more uniform distribution of the velocity values, that can be noticed by the presence of a peaks in the frequency ratio curve. For the C set-up, that is characterized by higher value of the CoV , the frequency ratio curve is more uniform showing the presence of both zones characterized by high or low values of the velocity module.

Conclusions

In this work, an off-axis 2D-PIV technique has been applied for the first time to the investigation of the flow field in KSM. A processing method was proposed to obtain 3D information through 2D PIV by means of symmetric feature of KSM, as well to eliminate the influence of out-of-plane velocity vectors on the velocity measurements on the plane. The impacts of element combinations on pressure drop and velocity distribution were analyzed. Key conclusions are as follows:

- (1) Pressure drop of element combinations with inverse direction was significantly higher than the same turning direction. The pressure drop linearly increases with the element number.
- (2) High velocity peaks were close to the pipe wall. Furthermore, flow velocity decreased approaching the center of KSM, and there were weaker peaks with opposite tangential velocity direction in the center of the cross section.
- (3) Upstream elements had different influences on final flow distribution according to different turning direction (clockwise or anticlockwise). Combination of two elements was beneficial to increase uniformity of velocity distribution, and the effect of inverse elements was more consistent.
- (4) Tangential velocity and axial velocity were the stronger components that determined the 2D velocity magnitude distribution and the 3D velocity magnitude distribution, respectively.

Authors' Contributions **Yao Zechen**: Methodology; experimental campaign; writing original draft. **Federico Alberini**: supervision; conceptualization; investigation; writing review and editing. **Giuseppina Montante**: conceptualization; supervision; writing review and editing. **Alessandro Paglianti**: conceptualization; supervision; writing review and editing.

Funding Open access funding provided by Alma Mater Studiorum - Università di Bologna within the CRUI-CARE Agreement. Z. C. Yao gratefully acknowledges the financial support for his stay at the University of Bologna from Fundamental Research Funds for the Central Universities, CHD, China (300102251711) and China Scholarship Council, China (202006560027).

Data Availability Not applicable.

Declarations

Ethical Approval Not applicable.

Competing Interests The authors declare that they have no conflict of interest.

Open Access This article is licensed under a Creative Commons Attribution 4.0 International License, which permits use, sharing, adaptation, distribution and reproduction in any medium or format, as long as you give appropriate credit to the original author(s) and the source, provide a link to the Creative Commons licence, and indicate if changes were made. The images or other third party material in this article are included in the article's Creative Commons licence, unless indicated otherwise in a credit line to the material. If material is not included in the article's Creative Commons licence and your intended use is not permitted by statutory regulation or exceeds the permitted use, you will need to obtain permission directly from the copyright holder. To view a copy of this licence, visit <http://creativecommons.org/licenses/by/4.0/>.

References

- Hosseini SM, Razzaghi K, Shahraki F (2019) Design and characterization of a low-pressure-drop static mixer. *AIChE J* 65:1126–1133. <https://doi.org/10.1002/aic.16505>
- Thakur RK, Vial C, Nigam KDP, Nauman EB, Djelveh G (2003) Static mixers in the process industries - a review. *Chem Eng Res Des* 81:787–826. <https://doi.org/10.1205/026387603322302968>
- Anxionnaz Z, Cabassud M, Gourdon C, Tochon P (2008) Heat exchanger/reactors (HEX reactors): concepts, technologies: state-of-the-art. *Chem Eng Process* 47:2029–2050. <https://doi.org/10.1016/j.cep.2008.06.012>
- Bayat M, Rahimpour MR, Taheri M, Pashaei M, Sharifzadeh S (2012) A comparative study of two different configurations for exothermic-endothermic heat exchanger reactor. *Chem Eng Process* 52:63–73. <https://doi.org/10.1016/j.cep.2011.11.010>
- Ferrouillat S, Tochon P, Garnier C, Peerhossaini H (2006) Intensification of heat-transfer and mixing in multifunctional heat exchangers by artificially generated streamwise vorticity. *Appl Therm Eng* 26:1820–1829. <https://doi.org/10.1016/j.applthermaleng.2006.02.002>
- Ferrouillat S, Tochon P, Peerhossaini H (2006) Micromixing enhancement by turbulence: application to multifunctional heat exchangers. *Chem Eng Process* 45:633–640. <https://doi.org/10.1016/j.cep.2006.01.006>
- Ghanem A, Lemenand T, Della Valle D, Peerhossaini H (2014) Static mixers: mechanisms, applications, and characterization methods - a review. *Chem Eng Res Des* 92:205–228. <https://doi.org/10.1016/j.cherd.2013.07.013>
- Shi H, Wang Y, Ge W, Fang B, Huggins JT, Huber TR, Zakin JL (2011) Enhancing heat transfer of drag-reducing surfactant solution by an HEV static mixer with low pressure drop. *Adv Mech Eng* 3:315943. <https://doi.org/10.1155/2011/315943>
- Wang C, Liu H, Yang X, Wang R (2021) Research for a non-standard kenics static mixer with an eccentricity factor. *Processes* 9:1353. <https://doi.org/10.3390/pr9081353>
- Morris WD, Misson P (1974) An experimental investigation of mass transfer and flow resistance in the Kenics static mixer. *Ind Eng Chem Process Des Dev* 13:270–275. <https://doi.org/10.1021/i260051a014>
- Morris WD, Benyon J (1976) Turbulent mass transfer in the Kenics static mixer. *Ind Eng Chem Process Des Dev* 15:338–342. <https://doi.org/10.1021/i260058a021>
- Pustelnik P (1986) Investigation of residence time distribution in Kenics static mixers. *Chem Eng Process* 20:147–154. [https://doi.org/10.1016/0255-2701\(86\)85019-X](https://doi.org/10.1016/0255-2701(86)85019-X)
- Kemblowski Z, Pustelnik P (1988) Residence time distribution of a power-law fluid in Kenics static mixers. *Chem Eng Sci* 43:473–478. [https://doi.org/10.1016/0009-2509\(88\)87008-8](https://doi.org/10.1016/0009-2509(88)87008-8)
- Ling FH, Zhang X (1995) A numerical study on mixing in the Kenics static mixer. *Chem Eng Commun* 136:119–141. <https://doi.org/10.1080/00986449508936357>
- Avalosse T, Crochet MJ (1997) Finite-element simulation of mixing: 2. Three-dimensional flow through a Kenics mixer. *AIChE J* 43:588–597. <https://doi.org/10.1002/aic.690430304>
- Hobbs DM, Muzzio FJ (1997) The Kenics static mixer: a three-dimensional chaotic flow. *Chem Eng J* 67:153–166. [https://doi.org/10.1016/S1385-8947\(97\)00013-2](https://doi.org/10.1016/S1385-8947(97)00013-2)
- Hobbs DM, Muzzio FJ (1998) Reynolds number effects on laminar mixing in the Kenics static mixer. *Chem Eng J* 70:93–104. [https://doi.org/10.1016/S1385-8947\(98\)00065-5](https://doi.org/10.1016/S1385-8947(98)00065-5)
- Hobbs DM, Swanson PD, Muzzio FJ (1998) Numerical characterization of low Reynolds number flow in the Kenics static mixer. *Chem Eng Sci* 53:1565–1584. [https://doi.org/10.1016/S0009-2509\(97\)00132-2](https://doi.org/10.1016/S0009-2509(97)00132-2)
- Jaffer SA, Wood PE (1998) Quantification of laminar mixing in the Kenics static mixer: an experimental study. *Can J Chem Eng* 76:516–521. <https://doi.org/10.1002/cjce.5450760323>
- Coroneo M, Montante G, Paglianti A (2012) Computational fluid dynamics modeling of corrugated static mixers for turbulent applications. *Ind Eng Chem Res* 51:15986–15996. <https://doi.org/10.1021/ie300398z>
- Van Wageningen WFC, Kandhai D, Mudde RF, Van Den Akker HEA (2004) Dynamic flow in a kenics static mixer: an assessment of various CFD methods. *AIChE J* 50:1684–1696. <https://doi.org/10.1002/aic.10178>
- Song HS, Han SP (2005) A general correlation for pressure drop in a Kenics static mixer. *Chem Eng Sci* 60:5696–5704. <https://doi.org/10.1016/j.ces.2005.04.084>
- Kumar V, Shirke V, Nigam KDP (2008) Performance of Kenics static mixer over a wide range of Reynolds number. *Chem Eng J* 139:284–295. <https://doi.org/10.1016/j.cej.2007.07.101>
- Lisboa PF, Fernandes J, Simões PC, Mota JPB, Saadatian E (2010) Computational-fluid-dynamics study of a Kenics static mixer as a heat exchanger for supercritical carbon dioxide. *J Supercrit Fluids* 55:107–115. <https://doi.org/10.1016/j.supflu.2010.08.005>
- Meng H, Zhu G, Yu Y, Wang Z, Wu J (2016) The effect of symmetrical perforated holes on the turbulent heat transfer in the static mixer with modified Kenics segments. *Int J Heat Mass Transf* 99:647–659. <https://doi.org/10.1016/j.ijheatmasstransfer.2016.03.110>
- Jiang X, Xiao Z, Jiang J, Yang X, Wang R (2021) Effect of element thickness on the pressure drop in the Kenics static mixer. *Chem Eng J* 424:130399. <https://doi.org/10.1016/j.cej.2021.130399>
- Nyande BW, Mathew Thomas K, Lakerveld R (2021) CFD analysis of a Kenics static mixer with a low pressure drop under laminar flow conditions. *Ind Eng Chem Res* 60:5264–5277. <https://doi.org/10.1021/acs.iecr.1c00135>
- Peryt-Stawiarska S, Jaworski Z (2008) Fluctuations of the non-Newtonian fluid flow in a Kenics static mixer: an experimental

- study. *Pol J Chem Technol* 10:35–37. <https://doi.org/10.2478/v10026-008-0033-3>
29. Murasiewicz H, Jaworski Z (2013) Investigation of turbulent flow field in a Kenics static mixer by Laser Doppler Anemometry. *Chem Pap* 67:1188–1200. <https://doi.org/10.2478/s11696-013-0375-z>
 30. Alberini F, Simmons MJH, Ingram A (2014) Use of an areal distribution of mixing intensity to describe blending of non-newtonian fluids in a Kenics KM static mixer using PLIF. *AIChE J* 60:332–342. <https://doi.org/10.1002/aic>
 31. Alberini F, Simmons MJH, Ingram A, Stitt EH (2014) Assessment of different methods of analysis to characterise the mixing of shear-thinning fluids in a Kenics KM static mixer using PLIF. *Chem Eng Sci* 112:152–169. <https://doi.org/10.1016/j.ces.2014.03.022>
 32. Ramsay J, Simmons MJH, Ingram A, Stitt EH (2016) Mixing performance of viscoelastic fluids in a Kenics KM in-line static mixer. *Chem Eng Res Des* 115:310–324. <https://doi.org/10.1016/j.cherd.2016.07.020>
 33. Rafiee M, Simmons MJH, Ingram A, Stitt EH (2013) Development of positron emission particle tracking for studying laminar mixing in Kenics static mixer. *Chem Eng Res Des* 91:2106–2113. <https://doi.org/10.1016/j.cherd.2013.05.022>
 34. Paglianti A, Montante G (2020) Simultaneous measurements of liquid velocity and tracer concentration in a continuous flow stirred tank. *Chem Eng Sci* 216:115495. <https://doi.org/10.1016/j.ces.2020.115495>
 35. Shi S, Zhang M, Fan X, Chen D (2015) Experimental and computational analysis of the impeller angle in a flotation cell by PIV and CFD. *Int J Miner Process* 142:2–9. <https://doi.org/10.1016/j.minpro.2015.04.029>
 36. Zou Y, Ye SS, Wang YD, Fei WY (2016) CFD simulation and PIV measurement of liquid-liquid two-phase flow in pump-mix mixer. *J Taiwan Inst Chem Eng* 60:15–25. <https://doi.org/10.1016/j.jtice.2015.10.007>
 37. Yoon JH, Lee SJ (2002) Direct comparison of 2D PIV and stereoscopic PIV measurements. *Meas Sci Technol* 13:1631–1642. <https://doi.org/10.1088/0957-0233/13/10/317>
 38. Noto D, Tasaka Y (2021) Dual-plane ensemble correlation for pixelwise 2D–3C velocity field measurements using a single camera. *Exp Fluids* 62:111. <https://doi.org/10.1007/s00348-021-03208-5>
 39. Xiong J, Aguirre-Pablo AA, Idoughi R, Thoroddsen ST, Heidirch W (2020) RainbowPIV with improved depth resolution - design and comparative study with TomoPIV. *Meas Sci Technol* 32:025401. <https://doi.org/10.1088/1361-6501/abb0ff>
 40. Barnkob R, Rossi M (2020) General defocusing particle tracking: fundamentals and uncertainty assessment. *Exp Fluids* 61(4):110. <https://doi.org/10.1007/s00348-020-2937-5>
 41. Cierpka C, Kähler CJ (2012) Particle imaging techniques for volumetric three-component (3D3C) velocity measurements in microfluidics. *J Vis* 15:1–31. <https://doi.org/10.1007/s12650-011-0107-9>
 42. Willert CE, Gharib M (1992) Three-dimensional particle imaging with a single camera. *Exp Fluids* 12:353–358. <https://doi.org/10.1007/BF00193880>
 43. Paglianti A, Montante G (2013) A mechanistic model for pressure drops in corrugated plates static mixers. *Chem Eng Sci* 97(2013):376–384. <https://doi.org/10.1016/j.ces.2013.04.042>
 44. Forte G, Brunazzi E, Alberini F (2019) Effect of residence time and energy dissipation on drop size distribution for the dispersion of oil in water using KMS and SMX+ static mixer. *Chem Eng Res Des* 148:417–428. <https://doi.org/10.1016/j.cherd.2019.06.021>
 45. Dantec (2002) Dantec Dynamic, FlowManager software and Introduction to PIV Instrumentation, Software User's guide. 2002
 46. Meng H, Zhu G, Yu Y, Wang Z, Wu J (2021) CFD-PBM numerical study on liquid-liquid dispersion in the Q-type static mixer. *Ind Eng Chem Res* 60:18121–18135. <https://doi.org/10.1021/acs.iecr.1c02906>
 47. Jiang X, Yang N, Wang R (2021) Effect of aspect ratio on the mixing performance in the Kenics static mixer. *Processes* 9(464):1–13. <https://doi.org/10.3390/pr9030464>
 48. Haddadi MM, Hosseini SH, Rashtchian D, Ahmadi G (2020) CFD modeling of immiscible liquids turbulent dispersion in Kenics static mixers: focusing on droplet behavior. *Chin J Chem Eng* 28:348–361. <https://doi.org/10.1016/j.cjche.2019.07.020>

Publisher's Note Springer Nature remains neutral with regard to jurisdictional claims in published maps and institutional affiliations.